catalysts

MDPI

Article

Synthesis of All-Inorganic Halide Perovskite Nanocrystals for Potential Photoelectric Catalysis Applications

Xiaoqian Wang, Wanli Liu, Jiazhen He, Yuqing Li and Yong Liu *

International School of Materials Science and Engineering (ISMSE), State Key Laboratory of Advanced Technology for Materials Synthesis and Processing, Wuhan University of Technology, Wuhan 430070, China; 303568@whut.edu.cn (X.W.); liuwani97@163.com (W.L.); jiazhenhe0606@163.com (J.H.); lyqlosyimi@163.com (Y.L.)
* Correspondence: liuyong3873@whut.edu.cn

Abstract: Compared with conventional semiconductors, halide perovskite nanocrystals (NCs) have a unique crystal structure and outstanding optoelectronic properties, offering wide potential for applications in optoelectronic devices such as solar cells, photodetectors, light-emitting diodes, lasers, and displays. Rational technological design is providing vital support for the development of perovskite optoelectronics. Herein, monodisperse all-inorganic halide perovskite nanocrystals with consistent morphology and cubic crystal phase were synthesized employing a modified one-pot hot injection method to independently modulate the stoichiometric ratios of three precursors involving cesium salt, lead source, and halide. In combination with an anion exchange reaction, mixing two kinds of perovskite NCs with different halogens enables a transition from violet emission to green and finally to red emission over the entire visible region. Additionally, optical and electrochemical tests suggested that the as-synthesized halide perovskite NCs are promising for photoelectric catalysis applications.

Keywords: synthesis; $CsPbX_3$; perovskite nanocrystals

check for updates

Citation: Wang, X.; Liu, W.; He, J.; Li, Y.; Liu, Y. Synthesis of All-Inorganic Halide Perovskite Nanocrystals for Potential Photoelectric Catalysis Applications. *Catalysts* **2023**, *13*, 1041. https://doi.org/10.3390/catal13071041

Academic Editor: Omid Akhavan

Received: 5 June 2023
Revised: 22 June 2023
Accepted: 24 June 2023
Published: 27 June 2023

Copyright: © 2023 by the authors. Licensee MDPI, Basel, Switzerland. This article is an open access article distributed under the terms and conditions of the Creative Commons Attribution (CC BY) license (https://creativecommons.org/licenses/by/4.0/).

1. Introduction

Over the past years, halide perovskite materials have developed dramatically as a novel solution-processable ionic semiconductor with a direct band gap. They possess a unique structure compared to conventional semiconductors, which can be expressed as ABX_3 (X = Cl^-, Br^-, I^-) [1]. The A-site is a monovalent cation with a relatively small radius, which can be Cs^+, ($CH_3NH_3^+$) MA^+, or ($[HC(NH_2)_2]^+$) FA^+, the B-site is occupied by divalent metal cations such as Pb^{2+} and Sn^{2+}, and the X-site is a halogen anion [2–6]. In the cubic halide perovskite crystal structure, six X^- and B^{2+} are connected to create a covalent top-linked $[BX_6]^{4-}$ coordinated octahedron B-site ion located at the octahedral center, while the A-site cation populates octahedral vacancies, which enables charge balance [7].

The structure of halide perovskite allows it to display superior optoelectronic properties, including a high absorption coefficient, extremely large photoluminescence quantum yield (PLQY), pure color emission, and variable band gap [8–10]. Among these properties, the PLQY of the red-emitting $CsPbI_3$ is already close to 100% [11]. Owing to its soft ionic nature and strongly ionic interactions with surface ligands, it allows for facile anion exchange to occur between perovskite nanocrystals (NCs) of different halogens, which can be utilized for flexible band-gap width modulation (1.78–3.1 eV) and control of the fluorescence wavelength covering the entire visible spectral range [9,12]. In addition, the enhanced quantum confinement effect of halide perovskite can be harnessed to tailor optical absorption and luminescence performance [13]. Electrically, halide perovskite is characterized by long charge diffusion lengths and high carrier mobility [14,15]. By means of time-resolved terahertz spectroscopy $CsPbBr_3$ NCs have been found to possess excellent free carrier performance, with carrier mobilities of up to 4500 $cm^2\ V^{-1}\ s^{-1}$ and diffusion lengths greater than 9.2 μm, making for ideal intrinsic transport properties [14]. Thus, halide perovskite holds great value for optoelectronic applications and offers a wide scope

of prospects in high-efficiency solar cells [16–18], sensitive photodetectors [19–21], low-threshold lasers [22–24], light-emitting diodes (LEDs) [25–27], scintillators [28–30], and bioimaging systems [31–33]. Among the multitude of applications, metal halide perovskite is particularly impressive in the field of solar cells. In the short span of about a decade, photoelectric conversion efficiency (PCE) has increased from an initial 3.8% to 25.5%, comparable to mature silicon-based solar cells [16]. As a result of these developments, halide perovskites now provide the ability to separate electron–hole pairs, and can be employed in the area of photoelectric catalysis applications [34–42].

The superior stability of all-inorganic $CsPbX_3$ perovskite materials compared to organic-inorganic hybrid halide perovskites is attributed to the sensitivity of organic molecules (such as MA^+) to light, heat, moisture, and irradiation, which decompose or damage the structure, limiting its application in storage, fabrication, and equipment manipulation processes [43–45]. The choice of synthesis technique likewise has an impact on the stability of the material. Until now, methods for the direct synthesis of all-inorganic perovskite comprised both solution-processed and vapor phase methods. The vapor phase method deposits single perovskite crystals or arrays on a substrate through a process of high temperature reactions [46,47], while solution-based processes aim to regulate the size and dimension of the halide perovskites by controlling technical parameters such as precursors, the amount of surface ligands, and the chemical reaction temperature and duration [48,49]. Nanoscale perovskite materials are a prerequisite for high performance optoelectronic applications. There are numerous approaches to the synthesis of promising NCs, with the ligand-assisted reprecipitation, solvothermal, and hot injection methods being effective and proven strategies. The synthesis protocol of the solvothermal method is relatively simple and controllable [50]. The precursors are usually mixed with a non-aqueous solvent and kept in a closed container such as a stainless steel autoclave, where cesium acetate (cesium oleate) and halide lead react to produce $CsPbX_3$ NCs under a certain temperature and self-generated pressure of the solution [51]. The ligand-assisted reprecipitation approach is based on the recrystallization of ligand halide salts, in which the metal halide salt is dissolved in a polar solvent and subsequently dropped into a nonpolar medium in the presence of the ligand to trigger the recrystallization of NCs [52]. In general, the hot injection method involves the synthesis of NCs by injecting cesium oleate into a lead halide solution under an inert atmosphere [8]. The aforementioned approaches are restricted in that the PbX_2 is applied as the lead and halogen sources, which makes it impossible to directly adjust the stoichiometric ratios of the two elements individually. The result is that the NCs are susceptible to damage through irradiation and are less stable under transmission electron microscopy [53,54]. Hence, improved hot injection methods are essential to govern the structural stability and optoelectronic properties of all-inorganic halide perovskite NCs.

Here, we employ a modified one-pot hot injection method to synthesize monodisperse and uniformly sized $CsPbX_3$ perovskite nanocrystals (NCs) by independently manipulating the stoichiometric ratios of Cs^+, Pb^{2+}, and X^-. Their cubic crystal structure and high phase purity were demonstrated by XRD analysis. The findings of Fourier transform infrared spectroscopy (FTIR) revealed the validated protonation of oleylamine on the surface of the $CsPbBr_3$ nanocrystals. In addition, the presence of a single narrow emission peak in the fluorescence spectra of the perovskite nanocrystals is driven by different halogen compositions, giving rise to varying band gaps and consequently differential fluorescence absorption and emission peak positions. Accompanied by the red shift of the fluorescence wavelength (narrowing of the band gap), the PL lifetime of the $CsPbCl_3$, $CsPbBr_3$, and $CsPbI_3$ NCs grow larger and their decay rate slows. The mixture of NCs with different halogens is susceptible to anion exchange reactions, allowing the absorption peaks of the nanocrystals to be tuned from 400 nm to 700 nm and the color of the nanocrystals to be gradually tuned from violet to red under 365 nm UV lamp excitation, covering the entire visible range. Optical and electrochemical tests revealed that the all-inorganic halide perovskite materials are applicable for photoelectric catalysis applications.

2. Results and Discussion

Synthesis of all-inorganic halide perovskite nanocrystals (NCs) is crucial for effective implementation of superior performance in optoelectronic devices. In particular, the selection of suitable precursors and reaction conditions are vital factors influencing the quality of the NCs. For the common hot injection method, cesium oleate is injected into a solution of lead halide (PbX_2) for reaction to transform into perovskite [8]. Cesium oleate is prone to solidifying at room temperature, and needs to be preheated prior to the injection process. Thus, we take the option of incorporating benzoyl halides, injecting them into salt solutions of the metal cations Cs^+ and Pb^{2+}, which provides a halogen-rich environment while facilitating the effective protonation of oleylamine (OAm). In our typical synthetic process, Cs_2CO_3 and $Pb(CH_3COO)_2{\cdot}3H_2O$ were applied as the cesium source and lead source, respectively, while oleic acid (OA) and OAm were chosen as the surface ligands and 1-octadecene (ODE) was chosen as the solvent. The reaction system was kept under vacuum by removing excess air and water by evacuation at 130 °C for 1h. Subsequently, $CsPbI_3$, $CsPbBr_3$, and $CsPbCl_3$ NCs were immediately synthesized by metathesis reactions via rapid injection of benzoyl halides under N_2 at 165 °C, 170 °C, and 200 °C (Scheme 1; more details are provided in the Section 3). In contrast to the conventional hot injection method, this approach made it possible to produce well-distributed perovskite NCs as a result of the independent control of the stoichiometric ratios of origin of Cs^+, Pb^{2+}, and X^- instead of employing PbX_2 as both the lead and halogen sources. In addition, a series of subsequent centrifugation procedures facilitated the final hexane dispersed solution of monodisperse cubic NCs.

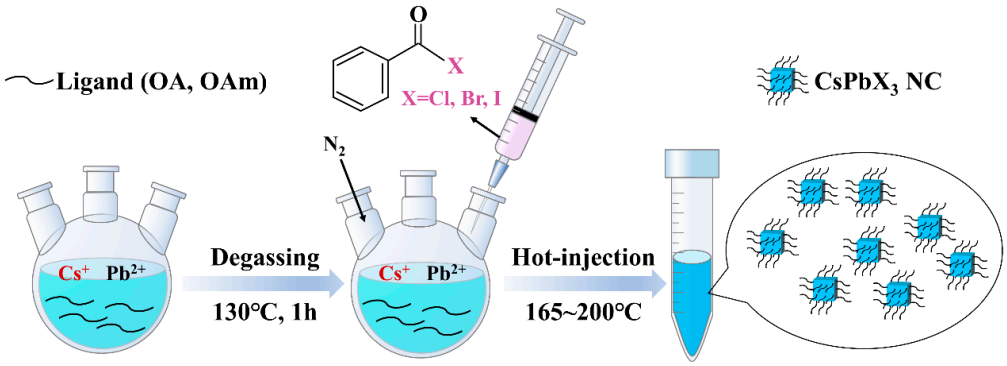

Scheme 1. Schematic diagram of the synthesis procedure of all-inorganic $CsPbX_3$ (X = Cl, Br, I) perovskite NCs.

As shown in Figure 1, TEM images of the $CsPbCl_3$, $CsPbBr_3$, and $CsPbI_3$ nanocrystals (NCs) display uniform and monodisperse cubic structures. Under electron microscopic irradiation, none of the three NCs instantly decomposed into white cubes and irregular black spots located in the corners, all keeping their shape and structure more integrated. Naturally, if irradiated in a continuous manner, the high-energy electron beam eventually damages the structure of the perovskite NCs; the decomposition products can include PbX_2, CsX, and CsPb [54]. It has been reported that the resistance of halide perovskite NCs to radiation exposure can be enhanced by supplementing the amount of halogen ions [55]. Our synthesis procedure is equipped with the ability to independently manipulate the stoichiometric ratio of the elements composing halide perovskite, which can effectively improve the irradiation stability of perovskite NCs. In addition to the halogen content, the temperature and electron beam dose have an influence on the morphology of all-inorganic halide perovskite. Incident electrons trigger the desorption of halogen ions from the $CsPbBr_3$ surface, which takes place with the evolution of the electron dose; moreover, low temperatures can be introduced to inhibit ion migration [54]. Therefore, in order to avoid or reduce radiation damage, it is possible to take measures such as changing the electronic irradiation dose and decreasing the working temperature of transmission

electron microscope (or directly employing cryo-electron microscopy) when capturing TEM images [56]. Additionally, 300 NCs were selected to measure their size, and analysis of the results indicated a concentrated distribution of sizes, with the average sizes being $CsPbCl_3$: 9.97 ± 0.20 nm, $CsPbBr_3$: 9.61 ± 0.13 nm, and $CsPbI_3$: 15.12 ± 0.14 nm. However, the sizes of the original nanocrystal particles were estimated by the Scherrer formula, $D = K\gamma/B\cos\theta$, at 8.85 nm, 9.51 nm, and 9.95 nm, respectively. Here, D is the grain size and K is the Scherrer constant; if B is the half-height width of the diffraction peak, then K = 0.89. Moreover, γ is the X-ray wavelength, typically 1.54056 Å for Cu kα; B is the half maximum full width (FWHM) of the diffraction peak of the measured sample; and θ is the Bragg diffraction angle. The reason for the difference in the results obtained by the two approaches is that the software was chosen and calculated in different ways.

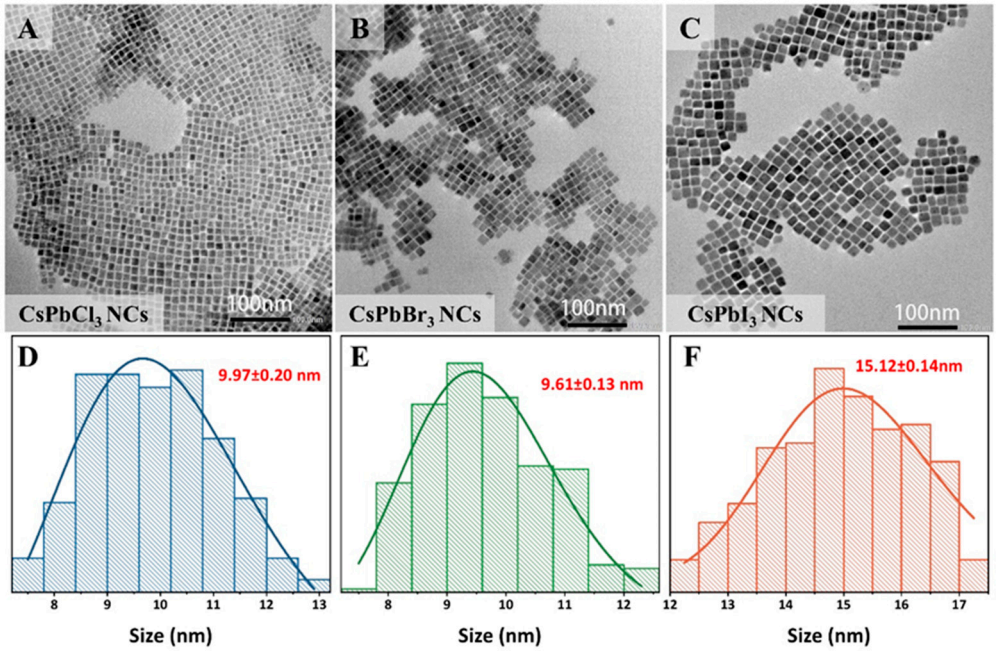

Figure 1. (**A**–**C**) TEM images of $CsPbCl_3$, $CsPbBr_3$, and $CsPbI_3$ NCs (scale bar: 100 nm) and (**D**–**F**) their size distribution diagrams.

X-ray diffraction (XRD) and Fourier transform infrared spectroscopy (FTIR) are methods for characterizing the structure and surface functional groups of materials. Figure 2A–C shows the XRD patterns obtained for the three different halogens of perovskite NCs, which were analyzed and well matched to cubic perovskite crystals. The corresponding ICSD numbers for the $CsPbCl_3$, $CsPbBr_3$, and $CsPbI_3$ NCs are 23108, 29073, and 181288, respectively, corresponding to the space group $pm\bar{3}m$ (No. 221). The diffraction peaks in the vicinity of $2\theta \approx 15°$, 20°, and 30° for all three types of perovskite nanocrystals correspond to the (100), (110), and (200) crystallographic planes. However, there is a notable divergence in the diffraction peak positions associated with the (210), (211), and (220) crystal planes of the NCs, with $CsPbCl_3$ at 35.8°, 39.3°, and 45.7°, respectively, whereas $CsPbBr_3$ is at 34.1°, 37.4°, and 43.5°, respectively, and $CsPbI_3$ near 31.9°, 35°, and 40.7°, respectively. The diffraction angles corresponding to the same diffraction crystal plane of the perovskite NCs change depending on the halogen component. From $CsPbCl_3$ to $CsPbBr_3$ to $CsPbI_3$, the diffraction peaks appear to be shifted in the direction of a small angle. Based on the Bragg equation, $2d\sin\theta = n\lambda$, where d is the spacing between crystal planes, θ is the diffraction half angle, and n is the diffraction order, XRD analysis of perovskite nanocrystals with heterogeneous halogen fractions was carried out and the results did not match the appropriate phases in the currently available card library. However, as shown in Figure S2, perovskite NCs with different halogen components all present only one set of diffraction peaks, instead of diffraction peaks of $CsPbBr_3$, $CsPbBr_xCl_{3-x}$ ($0 < x < 3$) (or $CsPbBr_yI_{3-y}$ ($0 < y < 3$),

and $CsPbCl_3$ (or $CsPbI_3$) at the same time. This demonstrates that only one material is ultimately present. In Figure S2A, the angle of the main diffraction peak tends to change at a smaller angle as the elemental content of Br (Cl) increases (decreases). Likewise, in Figure S2B the angle of the diffraction peak varies towards a smaller angle as the elemental content of I (Br) increases (decreases). In the FTIR spectrum of $CsPbBr_3$ NCs (Figure 2D), peak positions of 2925, 1379, and 2854 cm^{-1} can be observed, indicating asymmetric and symmetric stretching vibrations of the C–H single bond, respectively, while absorption peaks of 1466 and 721 cm^{-1} represent in-plane bending vibrations of the C–H single bond in the $–CH_2–$ group. The peaks at 993, 909, and 801 cm^{-1}, which originate from OA and OAm, represent the bending vibration of =C–H. The peak at 1536 cm^{-1} can be attributed to the C=O bond from the –COO– group of OA. In particular, the absorption peak located at a wave number of 1642 cm^{-1} denotes a deformational vibration of the N–H bond corresponding to $–NH_3^+$, which arises from the OAm. The appearance of differential absorption peak positions in the FTIR spectra is indicative of a variation in the vibrational mode of the functional groups, demonstrating the effective protonation of oleylamine on the surface of the $CsPbBr_3$ NCs.

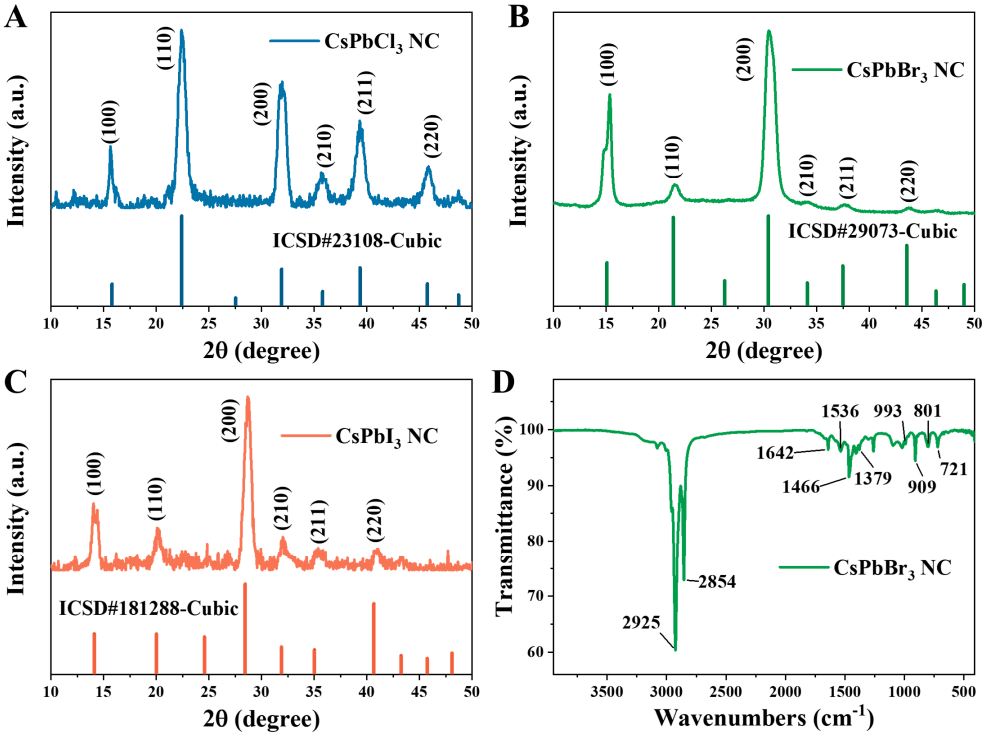

Figure 2. (**A**–**C**) XRD patterns of $CsPbX_3$ (X = Cl, Br, I) NCs and (**D**) FTIR spectra of $CsPbBr_3$ NCs.

The XPS spectra were employed to analyze the surface chemical valence states of the $CsPbCl_3$, $CsPbBr_3$, and $CsPbI_3$ NCs. The binding energy curves of Cs 3d and Pb 4f are recorded in Figure S2B,C. The peaks of Cs $3d_{5/2}$ and Cs $3d_{3/2}$ are located near 720 eV and 734 eV, respectively, and the peaks of Pb $4f_{7/4}$ and Pb $4f_{5/4}$ are located near 135 eV and 139 eV, corresponding to Cs^+ and Pb^{2+}. In Figure S2D–F, the coupled peaks located near 71 eV and 73 eV originate from Br $3d_{5/2}$ and Br $3d_{3/2}$, the strong peaks located near 194 eV and 196 eV are attributed to Cl $2p_{3/2}$ and Cl $2p_{1/2}$, and the peaks located at 615 eV and 627 eV originate from I $3d_{5/2}$ and I $3d_{3/2}$, corresponding to Br^-, Cl^-, and I^-, respectively. The full XPS spectra (Figure S2A) present the chemical elemental composition of $CsPbX_3$ (X = Cl, Br, I) NCs. The ratios of elemental content are Cs: Pb: Cl ≈ 1: 0.9: 2.2, Cs: Pb: Br ≈ 1: 1.7: 3.7, and Cs: Pb: I ≈ 1: 0.9: 2.2, respectively.

Later, we measured the fundamental optical properties of the three NCs, including the UV-vis absorption, PL, and TRPL spectra (Figure 3). The band edge peak positions

of the $CsPbCl_3$, $CsPbBr_3$, and $CsPbI_3$ NCs are found at 402 nm, 506 nm, and 675 nm, respectively. The absorption spectra exhibit two or three exciton leap peaks as a result of the quantum confinement effect, indicating the smaller size and better homogeneity of the all-inorganic perovskite NCs prepared by our scheme. The fluorescence emission peaks in the PL spectra are 411 nm, 521, nm and 694 nm, respectively, with the corresponding Stokes shifts due to quantum confinement effects calculated as 9 nm, 15 nm, and 19 nm, respectively. The average fluorescence lifetimes of $CsPbX_3$ (X = Cl, Br, I) NCs were 11.29 ns, 12.92 ns, and 49.26 ns, respectively, through a third-order exponential fitting from TRPL curves (Figure 3D). The different ionic radii of the three halogens Cl^-, Br^-, and I^- in turn become larger, leading to a variation in the volume of their vacancies in the perovskite crystal structure, which allows the optical band gap of the perovskite NCs to shift from $CsPbCl_3$ to $CsPbBr_3$ to $CsPbI_3$, becoming smaller in turn, with a corresponding gradual red shift in the fluorescence wavelength. Furthermore, only a narrow emission peak with a high photoluminescence quantum yield (PLQY) appears in the fluorescence spectrum. All-inorganic halide perovskite NCs possess huge potential for applications in semiconductor light-emitting devices such as light-emitting diodes and displays on account of their excellent optical properties.

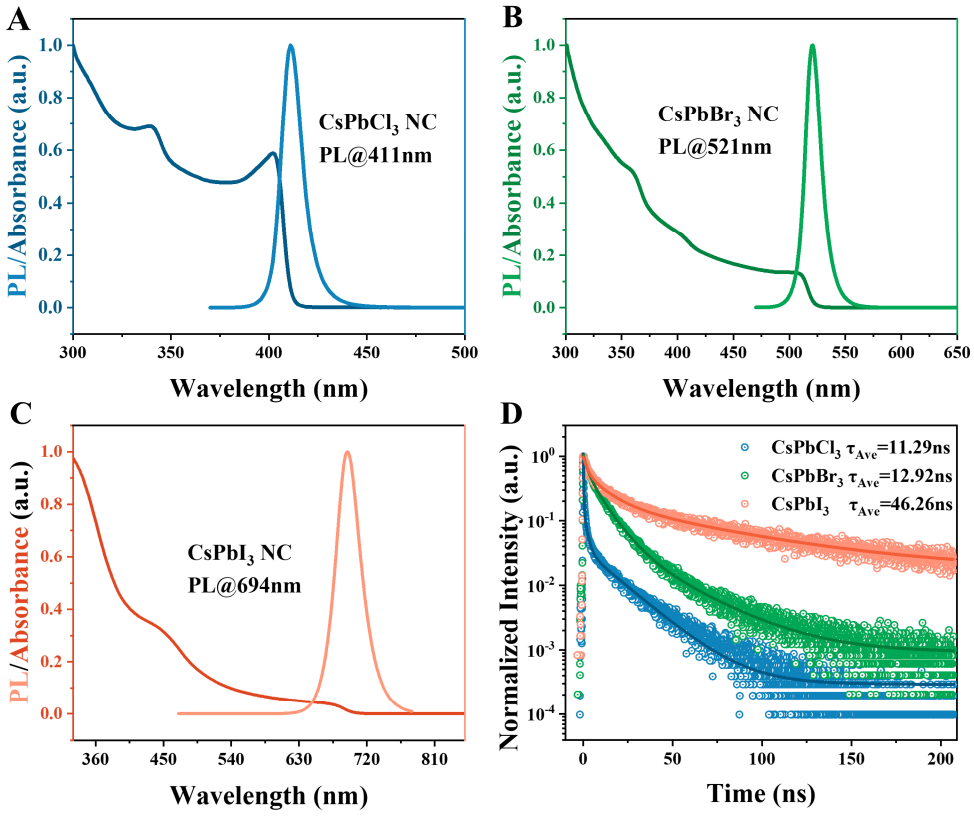

Figure 3. (**A**–**C**) UV-vis absorption and photoluminescence (PL) spectra of $CsPbCl_3$, $CsPbBr_3$, and $CsPbI_3$ NCs and (**D**) time-resolved photoluminescence (TRPL) spectra of $CsPbCl_3$, $CsPbBr_3$, and $CsPbI_3$ NCs. The small circles with a dot in the center represent raw data and the solid lines are the corresponding fitted curves.

In light of the ionic nature of perovskite and the variability of its surface ligands, anion exchange reactions readily occur between perovskite materials with diverse halogens. The common method adopted by researchers is to add metal halide salts of different halogens such as CuX_2 [57], KX [9], AlX_3 [58], and ZnX_2 [55] to perovskite NCs, then stir the mixture for a period of time before using centrifugal separation to obtain perovskite with different halogen components. Rather than following this approach, we instead mixed two types of perovskite nanocrystals with different halogens, achieving differences in luminescence

via ion exchange. The UV-vis spectra of the solutions of perovskite NCs with different halogen contents exhibit different absorption peak positions (Figure 4A). These solutions are composed of $CsPbCl_3$, $CsPbBr_3$ and $CsPbCl_3$ in volume ratios of 1:3 and 3:1, $CsPbBr_3$, $CsPbBr_3$ and $CsPbI_3$ in volume ratios of 3:1 and 1:3, $CsPbI_3$ NCs, corresponding to the positions of the respective leap peaks at 402 nm, 420 nm, 484 nm, 506 nm, 520 nm, 585 nm and 676 nm. Afterwards, based on the Einstein photoelectric effect and the Kubelka-Munk equation [59], the linear region of the absorption edge in the UV-Vis spectra was extrapolated to the energy axis intercept, which was used to estimate the surface optical band gaps of perovskite NCs with different halogen components as 3.03 eV, 2.84 eV, 2.49 eV, 2.37 eV, 2.33 eV, 2.02 eV, and 1.76 eV, respectively. Certain samples were observed to feature two sharp exciton absorption peaks, while others appeared to be relatively smooth, which we attributed to the varying extent of quantum confinement effects caused by differences in size, concentration, and homogeneity of the NCs. Perovskite nanocrystal solutions mixed in varying volume ratios behaved differently when stimulated with 365 nm UV lamps. As illustrated in Figure 4B, $CsPbCl_3$ NCs are purple, and gradually change to blue and then green as Br^- increases when mixed with $CsPbBr_3$, while $CsPbBr_3$ NCs are green and gradually change to yellow-orange and finally red $CsPbI_3$ as I^- increases when mixed with $CsPbI_3$. The mixing of $CsPbCl_3$ with $CsPbI_3$ NCs results in fluorescence extinction rather than fluorescence emission. According to our investigation, a plausible explanation is that the Cl^- and I^- radii are sufficiently distinct from each other that the mixing process may cause them to enter each other's crystal structures in such a way as to cause damage. Thus, there is no very effective means of making $CsPbCl_3$ coexist with $CsPbI_3$ while maintaining two different fluorescence emissions at the same time.

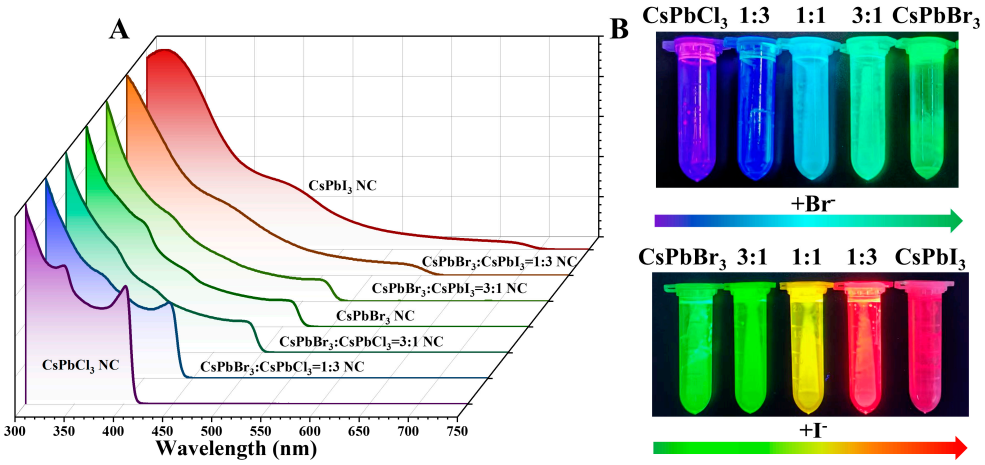

Figure 4. (**A**) UV-vis absorption spectra of perovskite NCs solutions with different volume ratios of $CsPbBr_3$ with $CsPbCl_3$, $CsPbBr_3$, and $CsPbI_3$; (**B**) image of mixed solutions of $CsPbBr_3$ and $CsPbCl_3$ NCs with different volume ratios and mixture of $CsPbBr_3$ and $CsPbI_3$ NCs with different volume ratios under 365 nm ultraviolet lamp excitation.

The states of the $CsPbX_3$ (X = Cl, Br, I) NCs in different solvents were compared, as shown in Figure S4. During these experiments, it was found that the NCs were more soluble in hexane than in water, and were more readily dispersed in hexane. The NCs dispersed in both solvents emitted light in similar colors under UV lamp irradiation. After one day, the $CsPbCl_3$ and $CsPbBr_3$ dispersed in water continued to emitted relatively strong light, while the $CsPbI_3$ NCs no longer emitted red light and behaved much less stably. The more stable $CsPbBr_3$ NCs were selected to test the photoresponse current density and electrochemical impedance spectra (EIS), as shown in Figure S5. The EIS spectra of $CsPbBr_3$ NCs exhibited a certain semicircular arc, indicating the presence of charge transfer resistance. In order to capture the photocurrent generated by the light signal and to exclude other influences, the photocurrent distribution is normally recorded at regular intervals when the light source is switched on. As depicted in Figure S5B, when the light source was switched

off, the recorded photocurrent density was almost zero, while when the light source was switched on again after 30 s, the current increased instantaneously. When the light source was switched off every 30 s, the current decreased instantaneously. This further confirms that the $CsPbBr_3$ perovskite material has suitable carrier migration efficiency with charge transport properties. Thus, $CsPbBr_3$ NCs could be promising in the field of photoelectric catalysis. Perovskite NCs with different halogen fractions feature diverse fluorescence emission and contribute to the construction of light-emitting diodes. Moreover, analogous to conventional semiconductor NCs, halide perovskite NCs exhibit good homogeneity and monodispersity along with a well-defined cubic shape, which might be promote self-assembly for use as building blocks in ordered superstructures such as superlattices. The degree of ordering of the perovskite superstructure affects the optoelectronic properties, and as such can be used to alter the performance of functional electronic devices.

3. Materials and Methods

3.1. Chemicals

Cesium carbonate (Cs_2CO_3, Aladdin, 99.9%), lead acetate trihydrate ($Pb(CH_3COO)_2 \cdot 3H_2O$, Aladdin, 99.99%), sodium iodide (NaI, Macklin, 99.99%), oleic acid (OA, Aladdin, AR), oleylamine (OAm, Aladdin, 80~90%), 1-octadecene (ODE, Aladdin, >90%(GC)), benzoyl bromide (C_6H_5COBr, Aladdin, 97%), benzoyl chloride (C_6H_5COCl, Aladdin, 99%), *n*-hexane (Aladdin, >99%). All reagents labeled Aladdin are from Aladdin Reagent (Shanghai) Co., Ltd., Shanghai, China. The reagent marked Macklin is from Shanghai Macklin Biochemical Co., Ltd., Shanghai, China.

3.2. Synthesis Scheme of All-Inorganic Perovskite Nanocrystals

3.2.1. Preparation of Benzoyl Iodine

The benzoyl iodine was synthesized following the method reported by Muhammad Imran. In a typical synthesis, sodium iodide (3 g, 0.2 mmol) and benzoyl chloride (1.4 mL) were mixed in a 20 mL vial. The mixture was stirred vigorously at 75 °C on a hot plate for 5 h. With heating and stirring, the mixture changed from white to orange red color, manifesting the successful synthesis of benzoyl iodine. Then, the mixture was gradually cooled to room temperature and 5 mL of anhydrous ODE was added to the vial. The solution was filtered by a polytetrafluorethylene membrane with a 0.45 μm pore size to obtain clear benzoyl iodine, which was stored in vacuum for further use.

3.2.2. Synthesis of $CsPbX_3$ (X = Cl, Br, I) Nanocrystals (NCs)

$CsPbX_3$ (X = Cl, Br, I) nanocrystals (NCs) were synthesized via the previously published procedure [60] with modifications. In a 50 mL three-necked round-bottom flask, 0.016 g Cs_2CO_3, 0.076 g $Pb(CH_3COO)_2 \cdot 3H_2O$, 0.3 mL OA, 1 mL OAm, and a variable amount of ODE (5 mL for $CsPbCl_3$ and $CsPbBr_3$ NCs, 8 mL for $CsPbI_3$ NCs) were loaded and dried under vacuum (−0.05~0.08 MPa) at 130 °C for 1 h. When the reaction mixture had solubilized completely, the flask was heated up to 165~200 °C under N_2 flow; (the specific reaction temperatures are 200 °C for $CsPbCl_3$ NCs, 170 °C for $CsPbBr_3$ NCs and 165 °C for $CsPbI_3$ NCs, respectively). Subsequently, benzoyl halides (1.8 mmol benzoyl chloride, 0.6 mmol benzoyl bromide, and 0.6 mmol benzoyl iodine) were swiftly injected. The reaction mixture was cooled immediately to room temperature using an ice bath for $CsPbBr_3$ and $CsPbI_3$ NCs, while the $CsPbCl_3$ NCs were cooled after 20 s to obtain crude solutions.

3.2.3. Isolation of $CsPbX_3$ (X = Cl, Br, I) Nanocrystals (NCs)

First, 5 mL of *n*-hexane was added to the $CsPbCl_3$ and $CsPbBr_3$ NC crude solutions, while 2 mL solvent was added to the $CsPbI_3$ NC solution. Next, the solution was centrifuged at 6000 rpm for 5 min. The supernatant was discarded and the precipitate was centrifuged again at 6000 rpm for 3 min without additional solvent; residual supernatant was removed with a paper tissue. Later, the precipitate was redispersed by adding 500 μL of *n*-hexane

and centrifuged again at 4000 rpm for 10min in order to separate larger particles. The resulting supernatants of $CsPbBr_3$ and $CsPbI_3$ NCs were collected, while the supernatant of the $CsPbCl_3$ NCs was discarded. Next, 2 mL *n*-hexane was loaded into the precipitate to redisperse the $CsPbCl_3$ NCs, followed by centrifuging at 4000 rpm for 10 min, and the supernatant was collected in a vial. Finally, $CsPbX_3$ (X = Cl, Br, I) NCs were diluted with *n*-hexane (500 μL, 1 mL, and 800 μL for $CsPbCl_3$, $CsPbBr_3$, and $CsPbI_3$ NCs, respectively).

3.2.4. Anion Exchange Reactions

In brief, $CsPbBr_3$ was mixed with $CsPbCl_3$ NCs taking different volume ratios. $CsPbBr_3$ was blended with $CsPbI_3$ NCs according to different volume ratios. When the anion exchange was complete, the solutions were transformed for 20~60 min into $CsPbBr_xCl_{3-x}$ ($0 < x < 3$) and $CsPbBr_yI_{3-y}$ ($0 < y < 3$) NCs, respectively.

3.3. Materials Characterization

3.3.1. Transmission Electron Microscopy (TEM) Characterization

TEM images were acquired on a JEOL JEM-1400 Plus electron microscope (JEOL, Beijing, China) equipped with a thermionic gun at an accelerating voltage of 120 kV. The samples of nanocrystals were prepared by depositing a diluted nanocrystal suspension in *n*-hexane onto carbon-coated copper grids. The size distribution images of NCs were calculated using Nano Measurer software version 1.02.0005.

3.3.2. X-ray Diffraction (XRD) Characterization

XRD analysis was recorded on a Bruker D8 ADVANCE X-ray diffractometer (Bruker, Karlsruhe, Germany) with Cu-Kα radiation (λ = 1.54056 Å, 40 kV and 40 mA). NC specimens for the XRD measurements were prepared by drop-casting a concentrated NC suspension in *n*-hexane onto a substrate of SiO_2/Si. XRD data analysis was conducted using Jade 6.5 software.

3.3.3. Fourier Transform Infrared (FTIR) Spectroscopy Characterization

Fourier transform infrared (FTIR) spectroscopy data were obtained utilizing a Nicolet 6700 Fourier transform infrared spectrometer (Thermo Fisher Scientific, Waltham, MA, USA) at room temperature. The wave number range of the instrument was set to 400 to 4000 cm^{-1}, the scanning speed was set to 1 time/s, and the maximum resolution was 0.019 cm^{-1}. According to the working principle of interferometer interference frequency modulation, the light emitted from the lamp is turned into interferometric light by a Michelson interferometer, then the interferometric light is allowed to irradiate the sample. The receiver receives the interferometric light, which contains information about the materials, which is then converted into a Fourier transform by the computer software to obtain a spectral diagram of the sample. For the test, a highly concentrated *n*-hexane dispersion solution of $CsPbBr_3$ perovskite nanocrystals was applied to a glass slice, left to dry, and then tested.

3.3.4. X-ray Photoelectron Spectroscopy (XPS) Characterization

The XPS spectra of perovskite nanocrystals were obtained using an AXIS SUPRA X-ray photoelectron spectrometer (Kratos Analytical, a Shimadzu Group Company, Manchester, UK) equipped with a Thermo Scientific Kα spectrometer and a monochromatic Al-Kα X-ray source. The data were converted to VGD format and processed utilizing Avantage software version 5.9922. The binding energy scale was internally referenced to the C1s peak (binding energy for C−C = 284.8 eV).

3.3.5. Fluorescence Spectrum Measurements

The UV-vis absorption spectra were carried out using a Shimadzu UV-1800 spectrophotometer with UVProbe 2.52 software. The steady-state photoluminescence (PL) spectra were measured on a Shimadzu RF-6000 spectrophotometer with LabSolutions RF software,

using an excitation wavelength (λ_{ex}) of 350 nm for $CsPbCl_3$ and 450 nm for $CsPbBr_3$ and $CsPbI_3$. Time-resolved photoluminescence spectra (TRPL) were collected via single photon counter. In the procedure of optical characterization, samples were prepared by diluting NCs solutions in *n*-hexane in quartz cuvettes with a path length of 10 mm.

3.3.6. (Photo) Electrochemistry Measurements

A Zennium electrochemical workstation (Kronach, Germany, Zahner Company) was used to obtain photocurrent and electrochemical impedance curves of halide perovskite NCs. The measurement was performed in a three-electrode setup with a working electrode of the sample, a platinum disk counter-electrode, and a reference electrode of Ag/AgCl (saturated KCl) ($E_{Ag/AgCl}$ = +0.1989V vs. NHE) in the (photo) electrochemical electrolyte (0.5 M Na_2SO_4). For photocurrent measurement, the light source was a 405 nm LED, and the light intensity was tested with a Newport photometer. Electrochemical impedance spectra were measured in 0.5 M Na_2SO_4 at −0.1 V vs. NHE with an amplitude of 10 mV (frequency: 100 mHz~20 kHz).

4. Conclusions

In conclusion, monodisperse all-inorganic halide perovskite nanocrystals (NCs) with a homogeneous cubic morphology, concentrated size distribution, and cubic crystal structure were synthesized using a modified hot injection method and independently modulating the ratios of cesium, lead, and halogen precursors. Moreover, we were able to achieve relevant information on the surface functional groups via FTIR spectroscopy, which demonstrated the effective protonation of OAm acting as a surface ligand. Different halogen components contribute to variations in the band gap of the perovskite NCs, and consequently to varying emission and absorption peak positions in the respective fluorescence spectra and UV-vis absorption spectra. Furthermore, in the fluorescence lifetime curve the fluorescence lifetime is larger, with a red shift of the fluorescence wavelength (band gap) and more slow decay. Nanocrystals mixed from distinct volume ratios undergo anion exchange reactions, and consequently exhibit various absorption peaks. In addition, the solution is capable of adjusting color from violet to green and from green to red under the stimulation of a UV lamp, covering essentially the entire visible light range. Photocurrent and electrochemical impedance tests indicate that our work can be expected to advance the potential of halide perovskite materials for photoelectric catalysis applications.

Supplementary Materials: The following supporting information can be downloaded at: https://www.mdpi.com/article/10.3390/catal13071041/s1, Figure S1: (A,B) XRD patterns of halide perovskite nanocrystals with different halogen composition; Figure S2: XPS spectra of $CsPbX_3$ (X = Cl, Br, I) nanocrystals. (A) Full spectra, (B) Cs 3d, (C) Pb 4f, (D) Cl 2p, (E) Br 3d, (F) I 3d; Figure S3: (A) UV-vis absorption spectra and (B) Absorbance versus photon energy and the determined bandgap E_g of halide perovskite nanocrystals with different halogen components. Figure S4: Images of $CsPbX_3$ (X = Cl, Br, I) nanocrystals in different solvent (water and *n*-hexane) under sunlight and 365 nm UV lamp, respectively; Figure S5: (A) Transient photocurrent responses to on-off illumination of $CsPbBr_3$ nanocrystals electrodes at −0.1 V versus NHE in neutral water (0.5 M Na_2SO_4). (B) Electrochemical impedance spectra (Nyquist plot) of $CsPbBr_3$ nanocrystals.

Author Contributions: Y.L. (Yong Liu) conceived the project and material synthetic design. X.W. and J.H. performed the experiments, sample testing, data collection, and analysis. X.W. and Y.L. (Yuqing Li) discussed the data and performed formal analyses. X.W., W.L. and Y.L. (Yong Liu) wrote, reviewed, and edited the manuscript. All authors have read and agreed to the published version of the manuscript.

Funding: This work was financially supported by the National Natural Science Foundation of China (52072281, Yong Liu), the Major Program of the National Natural Science Foundation of China (22293021, Yong Liu), and the National Innovation and Entrepreneurship Training Program for College Students (No. S202210497011, Yong Liu). Yong Liu gratefully acknowledges the Youth Innovation Research Fund project of the State Key Laboratory of Advanced Technology for Materials Synthesis and Processing, Wuhan University of Technology.

Data Availability Statement: Data are available in a publicly accessible repository that does not issue DOIs or on request from the corresponding author.

Acknowledgments: We are grateful to the School of Chemistry and Chemical and Life Sciences of Wuhan University of Technology for providing UV-Vis and PL characterization and to the Center for Materials Research and Analysis of Wuhan University of Technology Materials for FTIR testing.

Conflicts of Interest: The authors declare no conflict of interest.

References

1. Akkerman, Q.A.; Manna, L. What Defines a Halide Perovskite? *ACS Energy Lett.* **2020**, *5*, 604–610. [CrossRef] [PubMed]
2. Zhang, J.; Zhong, Y. Origins of p-Doping and Nonradiative Recombination in $CsSnI_3$. *Angew. Chem. Int. Ed. Engl.* **2022**, *61*, e202212002. [PubMed]
3. Saparov, B.; Mitzi, D.B. Organic-Inorganic Perovskites: Structural Versatility for Functional Materials Design. *Chem. Rev.* **2016**, *116*, 4558–4596. [CrossRef] [PubMed]
4. Ceratti, D.R.; Tenne, R.; Bartezzaghi, A.; Cremonesi, L.; Segev, L.; Kalchenko, V.; Oron, D.; Potenza, M.A.C.; Hodes, G.; Cahen, D. Self-Healing and Light-Soaking in $MAPbI_3$: The Effect of H_2O. *Adv. Mater.* **2022**, *34*, e2110239. [CrossRef] [PubMed]
5. Li, Y.; Ding, T.; Luo, X.; Tian, Y.; Lu, X.; Wu, K. Synthesis and Spectroscopy of Monodispersed, Quantum-Confined $FAPbBr_3$ Perovskite Nanocrystals. *Chem. Mater.* **2019**, *32*, 549–556. [CrossRef]
6. Seth, S.; Ahmed, T.; De, A.; Samanta, A. Tackling the Defects, Stability, and Photoluminescence of $CsPbX_3$ Perovskite Nanocrystals. *ACS Energy Lett.* **2019**, *4*, 1610–1618. [CrossRef]
7. Fu, Y.; Jiang, X.; Li, X.; Traore, B.; Spanopoulos, I.; Katan, C.; Even, J.; Kanatzidis, M.G.; Harel, E. Cation Engineering in Two-Dimensional Ruddlesden-Popper Lead Iodide Perovskites with Mixed Large A-Site Cations in the Cages. *J. Am. Chem. Soc.* **2020**, *142*, 4008–4021. [CrossRef]
8. Protesescu, L.; Yakunin, S.; Bodnarchuk, M.I.; Krieg, F.; Caputo, R.; Hendon, C.H.; Yang, R.X.; Walsh, A.; Kovalenko, M.V. Nanocrystals of Cesium Lead Halide Perovskites ($CsPbX_3$, X = Cl, Br, and I): Novel Optoelectronic Materials Showing Bright Emission with Wide Color Gamut. *Nano Lett.* **2015**, *15*, 3692–3696. [CrossRef]
9. Guhrenz, C.; Benad, A.; Ziegler, C.; Haubold, D.; Gaponik, N.; Eychmüller, A. Solid-State Anion Exchange Reactions for Color Tuning of $CsPbX_3$ Perovskite Nanocrystals. *Chem. Mater.* **2016**, *28*, 9033–9040. [CrossRef]
10. Akkerman, Q.A.; D'Innocenzo, V.; Accornero, S.; Scarpellini, A.; Petrozza, A.; Prato, M.; Manna, L. Tuning the Optical Properties of Cesium Lead Halide Perovskite Nanocrystals by Anion Exchange Reactions. *J. Am. Chem. Soc.* **2015**, *137*, 10276–10281. [CrossRef]
11. Liu, F.; Zhang, Y.; Ding, C.; Kobayashi, S.; Izuishi, T.; Nakazawa, N.; Toyoda, T.; Ohta, T.; Hayase, S.; Minemoto, T.; et al. Highly Luminescent Phase-Stable $CsPbI_3$ Perovskite Quantum Dots Achieving Near 100% Absolute Photoluminescence Quantum Yield. *ACS Nano* **2017**, *11*, 10373–10383. [CrossRef]
12. Liu, H.; Liu, Z.; Xu, W.; Yang, L.; Liu, Y.; Yao, D.; Zhang, D.; Zhang, H.; Yang, B. Engineering the Photoluminescence of $CsPbX_3$ (X = Cl, Br, and I) Perovskite Nanocrystals Across the Full Visible Spectra with the Interval of 1 nm. *ACS Appl. Mater. Interfaces* **2019**, *11*, 14256–14265. [CrossRef] [PubMed]
13. Jiang, Y.; Sun, C.; Xu, J.; Li, S.; Cui, M.; Fu, X.; Liu, Y.; Liu, Y.; Wan, H.; Wei, K.; et al. Synthesis-on-Substrate of Quantum Dot Solids. *Nature* **2022**, *612*, 679–684. [CrossRef] [PubMed]
14. Yettapu, G.R.; Talukdar, D.; Sarkar, S.; Swarnkar, A.; Nag, A.; Ghosh, P.; Mandal, P. Terahertz Conductivity within Colloidal $CsPbBr_3$ Perovskite Nanocrystals: Remarkably High Carrier Mobilities and Large Diffusion Lengths. *Nano Lett.* **2016**, *16*, 4838–4848. [CrossRef] [PubMed]
15. Zhang, X.; Xu, B.; Wang, W.; Liu, S.; Zheng, Y.; Chen, S.; Wang, K.; Sun, X.W. Plasmonic Perovskite Light-Emitting Diodes Based on the Ag-$CsPbBr_3$ System. *ACS Appl. Mater. Interfaces* **2017**, *9*, 4926–4931. [CrossRef]
16. Zhang, J.; Zhao, W.; Olthof, S.; Liu, S.F. Defects in $CsPbX_3$ Perovskite: From Understanding to Effective Manipulation for High-Performance Solar Cells. *Small Methods* **2021**, *5*, e2100725. [CrossRef]
17. Duan, C.; Cui, J.; Zhang, M.; Han, Y.; Yang, S.; Zhao, H.; Bian, H.; Yao, J.; Zhao, K.; Liu, Z.; et al. Precursor Engineering for Ambient-Compatible Antisolvent-Free Fabrication of High-Efficiency $CsPbI_2Br$ Perovskite Solar Cells. *Adv. Energy Mater.* **2020**, *10*, 2000691. [CrossRef]
18. Zhang, J.; Hodes, G.; Jin, Z.; Liu, S.F. All-Inorganic $CsPbX_3$ Perovskite Solar Cells: Progress and Prospects. *Angew. Chem. Int. Ed.* **2019**, *58*, 15596–15618. [CrossRef]
19. Ramasamy, P.; Lim, D.H.; Kim, B.; Lee, S.H.; Lee, M.S.; Lee, J.S. All-Inorganic Cesium Lead Halide Perovskite Nanocrystals for Photodetector Applications. *Chem. Commun.* **2016**, *52*, 2067–2070. [CrossRef]
20. He, Q.; Chen, G.; Wang, Y.; Liu, X.; Xu, D.; Xu, X.; Liu, Y.; Bao, J.; Wang, X. $CsPbX_3$-ITO (X = Cl, Br, I) Nano-Heterojunctions: Voltage Tuned Positive to Negative Photoresponse. *Small* **2021**, *17*, e2101403. [CrossRef]
21. Li, X.; Wang, Y.; Chen, T.; Xu, T.; Ye, S.; Liu, R.; Sun, Z.; Tan, C.; Lv, X.; Yang, J.; et al. Unencapsulated $CsPbClBr_2$ Film Photodetectors Grown by Thermal Vacuum Deposition Exhibit Exceptional Environmental Stability in High-Humidity Air. *ACS Appl. Energy Mater.* **2022**, *5*, 8709–8716. [CrossRef]

22. Wang, Z.; Yang, J.; Li, M.; Zeng, X.; Pi, M.; Liu, Z.; Liu, J.; Zhang, D.; Hu, Z.; Du, J. Low Threshold and Ultrastability of One-Step Air-Processed All-Inorganic $CsPbX_3$ Thin Films toward Full-Color Visible Amplified Spontaneous Emission. *ACS Appl. Mater. Interfaces* **2022**, *14*, 26904–26912. [CrossRef] [PubMed]
23. Nie, L.; Yu, X.; Ge, Y.; He, D.; Zhu, X.; Liu, H.; Guo, H.; Zhao, F.; Yu, S.; Qiu, J.; et al. Highly Stable and Controllable Lasing Actions from PVDF Encapsulated $CsPbBr_3$ Perovskite Microcrystals. *J. Mater. Chem. C* **2022**, *10*, 16301–16308. [CrossRef]
24. Wang, Y.; Li, X.; Nalla, V.; Zeng, H.; Sun, H. Solution-Processed Low Threshold Vertical Cavity Surface Emitting Lasers from All-Inorganic Perovskite Nanocrystals. *Adv. Funct. Mater.* **2017**, *27*, 1605088. [CrossRef]
25. Yang, X.; Zhang, X.; Deng, J.; Chu, Z.; Jiang, Q.; Meng, J.; Wang, P.; Zhang, L.; Yin, Z.; You, J. Efficient Green Light-Emitting Diodes Based on Quasi-Two-Dimensional Composition and Phase Engineered Perovskite with Surface Passivation. *Nat. Commun.* **2018**, *9*, 570. [CrossRef]
26. Cao, Y.; Wang, N.; Tian, H.; Guo, J.; Wei, Y.; Chen, H.; Miao, Y.; Zou, W.; Pan, K.; He, Y.; et al. Perovskite Light-Emitting Diodes Based on Spontaneously Formed Submicrometre-Scale Structures. *Nature* **2018**, *562*, 249–253. [CrossRef]
27. Lin, K.; Xing, J.; Quan, L.N.; de Arquer, F.P.G.; Gong, X.; Lu, J.; Xie, L.; Zhao, W.; Zhang, D.; Yan, C.; et al. Perovskite Light-emitting Diodes with External Quantum Efficiency Exceeding 20 Percent. *Nature* **2018**, *562*, 245–248. [CrossRef]
28. Wang, K.; Zhang, H.; Gu, Z. All-Inorganic Perovskite Nanocrystal Materials: New Generation of Scintillators for High Quality X-ray Imaging. *Sci. Bull.* **2019**, *64*, 1205–1206. [CrossRef]
29. Ma, W.; Jiang, T.; Yang, Z.; Zhang, H.; Su, Y.; Chen, Z.; Chen, X.; Ma, Y.; Zhu, W.; Yu, X.; et al. Highly Resolved and Robust Dynamic X-ray Imaging Using Perovskite Glass-Ceramic Scintillator with Reduced Light Scattering. *Adv. Sci.* **2021**, *8*, e2003728. [CrossRef]
30. Yang, H.; Li, H.; Yuan, R.; Chen, J.; Zhao, J.; Wang, S.; Liu, Y.; Li, Q.; Zhang, Z. A Novel Scintillation Screen for Achieving High-Energy Ray Detection with Fast and Full-Color Emission. *J. Mater. Chem. C* **2021**, *9*, 7905–7909. [CrossRef]
31. Chan, K.K.; Giovanni, D.; He, H.; Sum, T.C.; Yong, K.-T. Water-Stable All-Inorganic Perovskite Nanocrystals with Nonlinear Optical Properties for Targeted Multiphoton Bioimaging. *ACS Appl. Nano Mater.* **2021**, *4*, 9022–9033. [CrossRef]
32. Kar, M.R.; Kumar, S.; Acharya, T.K.; Goswami, C.; Bhaumik, S. Highly Water-Stable, Luminescent, and Monodisperse Polymer-Coated $CsPbBr_3$ Nanocrystals for Imaging in Living Cells with Better Sensitivity. *RSC Adv.* **2023**, *13*, 5946–5956. [CrossRef] [PubMed]
33. Mohapatra, A.; Kumar, S.; Acharya, T.K.; Goswami, C.; Bhaumik, S. Highly Stable Multi-Encapsulated Red-Emitting Cesium Lead Halide Nanocrystals for Efficient Copper Ion Detection and Imaging in Live Cells. *J. Alloys Compd.* **2023**, *947*, 169453. [CrossRef]
34. Xiao, M.; Hao, M.; Lyu, M.; Moore, E.G.; Zhang, C.; Luo, B.; Hou, J.; Lipton-Duffin, J.; Wang, L. Surface Ligands Stabilized Lead Halide Perovskite Quantum Dot Photocatalyst for Visible Light-Driven Hydrogen Generation. *Adv. Funct. Mater.* **2019**, *29*, 1905683. [CrossRef]
35. Yang, Y.; Li, Y.; Gong, W.; Guo, H.; Niu, X. Cobalt-doped $CsPbBr_3$ perovskite quantum dots for photoelectrocatalytic hydrogen production via efficient charge transport. *Colloids Surf. A* **2023**, *663*, 131083. [CrossRef]
36. Pavliuk, M.V.; Abdellah, M.; Sá, J. Hydrogen Evolution with $CsPbBr_3$ Perovskite Nanocrystals under Visible Light in Solution. *Mater. Today Commun.* **2018**, *16*, 90–96. [CrossRef]
37. Xu, Y.F.; Yang, M.Z.; Chen, B.X.; Wang, X.D.; Chen, H.Y.; Kuang, D.B.; Su, C.Y. A $CsPbBr_3$ Perovskite Quantum Dot/Graphene Oxide Composite for Photocatalytic CO_2 Reduction. *J. Am. Chem. Soc.* **2017**, *139*, 5660–5663. [CrossRef]
38. Hou, J.; Cao, S.; Wu, Y.; Gao, Z.; Liang, F.; Sun, Y.; Lin, Z.; Sun, L. Inorganic Colloidal Perovskite Quantum Dots for Robust Solar CO_2 Reduction. *Chemistry* **2017**, *23*, 9481–9485. [CrossRef]
39. Li, L.; Zhang, Z.; Ding, C.; Xu, J. Boosting charge separation and photocatalytic CO_2 reduction of $CsPbBr_3$ perovskite quantum dots by hybridizing with P3HT. *Chem. Eng. J.* **2021**, *419*, 129543. [CrossRef]
40. Liu, H.; Bansal, S. Metal halide perovskite nanostructures and quantum dots for photocatalytic CO_2 reduction: Prospects and challenges. *Mater. Today Energy* **2023**, *32*, 101230. [CrossRef]
41. Das, S.; Paul, T.; Maiti, S.; Chattopadhyay, K.K. Ambient Processed $CsPbX_3$ Perovskite Cubes for Photocatalysis. *Mater. Lett.* **2020**, *267*, 127501. [CrossRef]
42. Gao, G.; Xi, Q.; Zhou, H.; Zhao, Y.; Wu, C.; Wang, L.; Guo, P.; Xu, J. Novel inorganic perovskite quantum dots for photocatalysis. *Nanoscale* **2017**, *9*, 12032–12038. [CrossRef]
43. Xin, B.; Pak, Y.; Mitra, S.; Almalawi, D.; Alwadai, N.; Zhang, Y.; Roqan, I.S. Self-Patterned $CsPbBr_3$ Nanocrystals for High-Performance Optoelectronics. *ACS Appl. Mater. Interfaces* **2019**, *11*, 5223–5231. [CrossRef] [PubMed]
44. Fu, X.; Zhang, C.; Peng, Z.; Xia, Y.; Zhang, J.; Luo, W.; Zhan, R.; Li, H.; Wang, Y.; Zhang, D. Self-Assembly and Photoactivation of Blue Luminescent $CsPbBr_3$ Mesocrystals Synthesized at Ambient Temperature. *J. Mater. Chem. C* **2018**, *6*, 1701–1708. [CrossRef]
45. Liu, X.; Li, J.; Cui, X.; Wang, X.; Yang, D. Strategies for the Preparation of High-Performance Inorganic Mixed-Halide Perovskite Solar Cells. *RSC Adv.* **2022**, *12*, 32925–32948. [CrossRef] [PubMed]
46. Wang, Y.; Yasar, M.; Luo, Z.; Zhou, S.; Yu, Y.; Li, H.; Yang, R.; Wang, X.; Pan, A.; Gan, L.; et al. Temperature Difference Triggering Controlled Growth of All-Inorganic Perovskite Nanowire Arrays in Air. *Small* **2018**, *14*, e1803010. [CrossRef] [PubMed]
47. Dong, S.; Hu, Z.Y.; Wei, P.; Han, J.; Wang, Z.; Liu, J.; Su, B.L.; Zhao, D.; Liu, Y. All-Inorganic Perovskite Single-Crystal Photoelectric Anisotropy. *Adv. Mater.* **2022**, *34*, e2204342. [CrossRef] [PubMed]
48. Sun, S.; Yuan, D.; Xu, Y.; Wang, A.; Deng, Z. Ligand-Mediated Synthesis of Shape-Controlled Cesium Lead Halide Perovskite Nanocrystals via Reprecipitation Process at Room Temperature. *ACS Nano* **2016**, *10*, 3648–3657. [CrossRef]

49. Pan, A.; He, B.; Fan, X.; Liu, Z.; Urban, J.J.; Alivisatos, A.P.; He, L.; Liu, Y. Insight into the Ligand-Mediated Synthesis of Colloidal $CsPbBr_3$ Perovskite Nanocrystals: The Role of Organic Acid, Base, and Cesium Precursors. *ACS Nano* **2016**, *10*, 7943–7954. [CrossRef]
50. Chen, D.; Fang, G.; Chen, X.; Lei, L.; Zhong, J.; Mao, Q.; Zhou, S.; Li, J. Mn-Doped $CsPbCl_3$ Perovskite Nanocrystals: Solvothermal Synthesis, Dual-Color Luminescence and Improved Stability. *J. Mater. Chem. C* **2018**, *6*, 8990–8998. [CrossRef]
51. Chen, M.; Zou, Y.; Wu, L.; Pan, Q.; Yang, D.; Hu, H.; Tan, Y.; Zhong, Q.; Xu, Y.; Liu, H.; et al. Solvothermal Synthesis of High-Quality All-Inorganic Cesium Lead Halide Perovskite Nanocrystals: From Nanocube to Ultrathin Nanowire. *Adv. Funct. Mater.* **2017**, *27*, 1701121. [CrossRef]
52. Han, D.; Imran, M.; Zhang, M.; Chang, S.; Wu, X.G.; Zhang, X.; Tang, J.; Wang, M.; Ali, S.; Li, X.; et al. Efficient Light-Emitting Diodes Based on in Situ Fabricated $FAPbBr_3$ Nanocrystals: The Enhancing Role of the Ligand-Assisted Reprecipitation Process. *ACS Nano* **2018**, *12*, 8808–8816. [CrossRef]
53. Chen, X.; Wang, Z. Investigating Chemical and Structural Instabilities of Lead Halide Perovskite Induced by Electron Beam Irradiation. *Micron* **2019**, *116*, 73–79. [CrossRef] [PubMed]
54. Dang, Z.; Shamsi, J.; Akkerman, Q.A.; Imran, M.; Bertoni, G.; Brescia, R.; Manna, L. Low-Temperature Electron Beam-Induced Transformations of Cesium Lead Halide Perovskite Nanocrystals. *ACS Omega* **2017**, *2*, 5660–5665. [CrossRef] [PubMed]
55. Li, F.; Liu, Y.; Wang, H.; Zhan, Q.; Liu, Q.; Xia, Z. Postsynthetic Surface Trap Removal of $CsPbX_3$ (X = Cl, Br, or I) Quantum Dots via a ZnX_2/Hexane Solution toward an Enhanced Luminescence Quantum Yield. *Chem. Mater.* **2018**, *30*, 8546–8554. [CrossRef]
56. Yu, Y.; Zhang, D.; Kisielowski, C.; Dou, L.; Kornienko, N.; Bekenstein, Y.; Wong, A.B.; Alivisatos, A.P.; Yang, P. Atomic Resolution Imaging of Halide Perovskites. *Nano Lett.* **2016**, *16*, 7530–7535. [CrossRef]
57. Chen, Y.-C.; Chou, H.-L.; Lin, J.-C.; Lee, Y.-C.; Pao, C.-W.; Chen, J.-L.; Chang, C.-C.; Chi, R.-Y.; Kuo, T.-R.; Lu, C.-W.; et al. Enhanced Luminescence and Stability of Cesium Lead Halide Perovskite $CsPbX_3$ Nanocrystals by Cu^{2+}-Assisted Anion Exchange Reactions. *J. Phy. Chem. C* **2019**, *123*, 2353–2360. [CrossRef]
58. Uddin, M.A.; Glover, J.D.; Park, S.M.; Pham, J.T.; Graham, K.R. Growth of Highly Stable and Luminescent $CsPbX_3$ (X = Cl, Br, and I) Nanoplates via Ligand Mediated Anion Exchange of $CsPbCl_3$ Nanocubes with AlX_3. *Chem. Mater.* **2020**, *32*, 5217–5225. [CrossRef]
59. Zhang, Y.; Wang, X.; Chen, Y.; Gao, Y. Improved Electroluminescence Performance of Quantum Dot Light-Emitting Diodes: A Promising Hole Injection Layer of Fe-doped NiO Nanocrystals. *Opt. Mater.* **2020**, *107*, 110158. [CrossRef]
60. Imran, M.; Caligiuri, V.; Wang, M.; Goldoni, L.; Prato, M.; Krahne, R.; De Trizio, L.; Manna, L. Benzoyl Halides as Alternative Precursors for the Colloidal Synthesis of Lead-Based Halide Perovskite Nanocrystals. *J. Am. Chem. Soc.* **2018**, *140*, 2656–2664. [CrossRef]

Disclaimer/Publisher's Note: The statements, opinions and data contained in all publications are solely those of the individual author(s) and contributor(s) and not of MDPI and/or the editor(s). MDPI and/or the editor(s) disclaim responsibility for any injury to people or property resulting from any ideas, methods, instructions or products referred to in the content.